Journal of Astronomical Telescopes, Instruments, and Systems

AstronomicalTelescopes.SPIEDigitalLibrary.org

Design and performance of Soft Gamma-ray Detector onboard the Hitomi (ASTRO-H) satellite

Hiroyasu Tajima
Shin Watanabe
Yasushi Fukazawa
Roger Blandford
Teruaki Enoto
Andrea Goldwurm
Kouichi Hagino
Katsuhiro Hayashi
Yuto Ichinohe
Jun Kataoka
Jun'ichiro Katsuta
Takao Kitaguchi
Motohide Kokubun
Philippe Laurent
François Lebrun
Olivier Limousin
Grzegorz
M. Madejski
Kazuo Makishima
Tsunefumi Mizuno
Kunishiro Mori
Takeshi Nakamori
Toshio Nakano
Kazuhiro Nakazawa
Hirofumi Noda
Hirokazu Odaka
Masanori Ohno
Masayuki Ohta
Shinya Saito
Goro Sato
Rie Sato
Shin'ichiro Takeda
Hiromitsu Takahashi
Tadayuki Takahashi
Takaaki Tanaka
Yasuyuki Tanaka
Yukikatsu Terada
Hideki Uchiyama
Yasunobu Uchiyama
Kazutaka Yamaoka
Yoichi Yatsu
Daisuke Yonetoku
Takayuki Yuasa

Hiroyasu Tajima, Shin Watanabe, Yasushi Fukazawa, Roger Blandford, Teruaki Enoto, Andrea Goldwurm, Kouichi Hagino, Katsuhiro Hayashi, Yuto Ichinohe, Jun Kataoka, Jun'ichiro Katsuta, Takao Kitaguchi, Motohide Kokubun, Philippe Laurent, François Lebrun, Olivier Limousin, Grzegorz M. Madejski, Kazuo Makishima, Tsunefumi Mizuno, Kunishiro Mori, Takeshi Nakamori, Toshio Nakano, Kazuhiro Nakazawa, Hirofumi Noda, Hirokazu Odaka, Masanori Ohno, Masayuki Ohta, Shinya Saito, Goro Sato, Rie Sato, Shin'ichiro Takeda, Hiromitsu Takahashi, Tadayuki Takahashi, Takaaki Tanaka, Yasuyuki Tanaka, Yukikatsu Terada, Hideki Uchiyama, Yasunobu Uchiyama, Kazutaka Yamaoka, Yoichi Yatsu, Daisuke Yonetoku, Takayuki Yuasa, "Design and performance of Soft Gamma-ray Detector onboard the Hitomi (ASTRO-H) satellite," *J. Astron. Telesc. Instrum. Syst.* **4**(2), 021411 (2018), doi: 10.1117/1.JATIS.4.2.021411.

Design and performance of Soft Gamma-ray Detector onboard the Hitomi (ASTRO-H) satellite

Hiroyasu Tajima,[a,*] Shin Watanabe,[b] Yasushi Fukazawa,[c] Roger Blandford,[d,e,f] Teruaki Enoto,[g,h] Andrea Goldwurm,[i] Kouichi Hagino,[j] Katsuhiro Hayashi,[b,k] Yuto Ichinohe,[l] Jun Kataoka,[m] Jun'ichiro Katsuta,[c] Takao Kitaguchi,[c] Motohide Kokubun,[b] Philippe Laurent,[i,n] François Lebrun,[i] Olivier Limousin,[i] Grzegorz M. Madejski,[d] Kazuo Makishima,[o] Tsunefumi Mizuno,[c,p] Kunishiro Mori,[b] Takeshi Nakamori,[q] Toshio Nakano,[r] Kazuhiro Nakazawa,[s,t,†] Hirofumi Noda,[u,v] Hirokazu Odaka,[d] Masanori Ohno,[c] Masayuki Ohta,[b] Shinya Saito,[w] Goro Sato,[b] Rie Sato,[b] Shin'ichiro Takeda,[x,‡] Hiromitsu Takahashi,[c] Tadayuki Takahashi,[b,‡] Takaaki Tanaka,[y] Yasuyuki Tanaka,[c] Yukikatsu Terada,[z] Hideki Uchiyama,[aa] Yasunobu Uchiyama,[w] Kazutaka Yamaoka,[a,k] Yoichi Yatsu,[ab] Daisuke Yonetoku,[ac] and Takayuki Yuasa[o]

[a]Nagoya University, Institute for Space-Earth Environmental Research, Nagoya, Japan
[b]Japan Aerospace Exploration Agency, Institute of Space and Astronautical Science, Sagamihara, Japan
[c]Hiroshima University, School of Science, Higashi-Hiroshima, Japan
[d]Stanford University, Kavli Institute for Particle Astrophysics and Cosmology, Stanford, California, United States
[e]Stanford University, Department of Physics, Stanford, California, United States
[f]SLAC National Accelerator Laboratory, Menlo Park, California, United States
[g]Kyoto University, Department of Astronomy, Kyoto, Japan
[h]Kyoto University, The Hakubi Center for Advanced Research, Kyoto, Japan
[i]CEA Saclay, Gif sur Yvette, France
[j]Tokyo University of Science, Department of Physics, Chiba, Japan
[k]Nagoya University, Department of Physics, Nagoya, Japan
[l]Tokyo Metropolitan University, Department of Physics, Tokyo, Japan
[m]Waseda University, Research Institute for Science and Engineering, Tokyo, Japan
[n]Laboratoire APC, Paris, France
[o]Institute of Physical and Chemical Research, Wako, Japan
[p]Hiroshima University, Hiroshima Astrophysical Science Center, Higashi-Hiroshima, Japan
[q]Yamagata University, Faculty of Science, Yamagata, Japan
[r]RIKEN Nishina Center, Wako, Japan
[s]The University of Tokyo, Department of Physics, Tokyo, Japan
[t]The University of Tokyo, School of Science, Research Center for the Early Universe, Tokyo, Japan
[u]Tohoku University, Frontier Research Institute for Interdisciplinary Sciences, Sendai, Japan
[v]Tohoku University, Astronomical Institute, Sendai, Japan
[w]Rikkyo University, Department of Physics, Tokyo, Japan
[x]Okinawa Institute of Science and Technology Graduate University, Onna-son, Japan
[y]Kyoto University, Department of Physics, Kyoto, Japan
[z]Saitama University, Department of Physics, Saitama, Japan
[aa]Shizuoka University, Faculty of Education, Shizuoka, Japan
[ab]Tokyo Institute of Technology, Department of Physics, Tokyo, Japan
[ac]Kanazawa University, Faculty of Mathematics and Physics, Kanazawa, Japan

Abstract. Hitomi (ASTRO-H) was the sixth Japanese x-ray satellite that carried instruments with exquisite energy resolution of <7 eV and broad energy coverage of 0.3 to 600 keV. The Soft Gamma-ray Detector (SGD) was the Hitomi instrument that observed the highest energy band (60 to 600 keV). The SGD design achieves a low background level by combining active shields and Compton cameras where Compton kinematics is utilized to reject backgrounds coming from outside of the field of view. A compact and highly efficient Compton camera is realized using a combination of silicon and cadmium telluride semiconductor sensors with a good energy resolution. Compton kinematics also carries information for gamma-ray polarization, making the SGD an excellent polarimeter. Following several years of development, the satellite was successfully launched on February 17, 2016. After proper functionality of the SGD components were verified, the nominal observation mode was initiated on March 24, 2016. The SGD observed the Crab Nebula for approximately two hours before the spacecraft ceased to function on March 26, 2016. We present concepts of the SGD design followed by detailed description of the instrument and its performance measured on ground and in orbit. [DOI: 10.1117/1.JATIS.4.2.021411]

Keywords: gamma rays; x-rays; polarimeters; detectors; satellites; astronomy.

Paper 17050SS received Aug. 7, 2017; accepted for publication Mar. 19, 2018; published online Apr. 26, 2018.

*Address all correspondence to: Hiroyasu Tajima, E-mail: tajima@nagoya-u.jp

†Current address: Nagoya University, Department of Physics, Nagoya, Japan

‡Current address: The University of Tokyo, the University of Tokyo Institutes for Advanced Study, Kavli Institute for the Physics and Mathematics of the Universe (WPI), Chiba, Japan

1 Introduction

Hitomi was the sixth Japanese x-ray astronomy satellite[1–6] developed to investigate a variety of astrophysical problems, including the formation mechanisms and dynamics of galaxy clusters, formation and evolution of supermassive black holes, and to

uncover the behavior of matter under extreme conditions, such as high density, strong magnetic field, and strong gravity in the vicinity of neutron stars and black holes. To fulfill the above objectives, the Hitomi satellite carried the following instruments: a very high-energy-resolution soft x-ray spectrometer (SXS) covering the 0.3- to 12-keV band consisting of thin-foil x-ray optics [Soft X-ray Telescope (SXT)][7] and a microcalorimeter array (SXS);[8] a soft x-ray imaging spectrometer sensitive in the 0.4- to 12-keV band, consisting of an SXT focusing x-rays onto CCD sensors (Soft x-ray Imager);[9] a hard x-ray imaging spectrometer, sensitive in the 3- to 80-keV band, consisting of multilayer-coated, focusing hard x-ray mirrors (Hard X-ray Telescope)[10] and silicon (Si) and cadmium telluride (CdTe) cross-strip sensors [Hard X-ray Imager (HXI)];[11–20] and a soft gamma-ray spectrometer covering the 60- to 600-keV band, utilizing multilayer semiconductor Compton cameras with an active shield [Soft Gamma-ray Detector (SGD)].[11–14,21,22–25]

In the Hitomi mission, the wide-band spectroscopy was expected to play a central role in the investigation of supermassive back holes and physics under extreme conditions. The SGD provided spectral measurements in the highest end of the Hitomi energy band above the HXI's energy band. In addition, the SGD was expected to measure polarization of relatively bright sources at around 100 keV.

The SGD design was based on the success of the Hard X-ray Detector (HXD)[26,27–29] onboard Suzaku. The HXD consists of Si photodiodes and gadolinium oxyorthosilicate (GSO) scintillators with bismuth germanate (BGO) active shields and phosphor bronze passive collimators, and achieved the best sensitivity in the 15- to 200-keV band before NuSTAR was launched with focusing optics. The sensitivity of the HXD GSO was limited by gamma-ray backgrounds arising from the contamination of signal from celestial sources, and by background resulting from radiation by radioisotopes in the GSO scintillators and the activation of the detector materials mainly due to the particle environment of the South Atlantic Anomaly (SAA).

The design of the SGD attempted to reduce those internal backgrounds by employing direction-sensitive gamma-ray detectors made of semiconductor sensors. Semiconductor sensors are much less prone to contamination by radioisotopes and also have good energy resolution, allowing an identification of line-like gamma-ray backgrounds. Directional sensitivity can further suppress backgrounds by rejecting events that do not originate from within the field of view (FOV).

2 Instrument Concept

The mission-level science objectives described above specifically require the SGD to provide spectroscopy up to 600 keV for over 10 supermassive black holes with fluxes equivalent to 1/1000 of the Crab Nebula (as measured over the 2- to 10-keV band, assuming the spectrum to be a power-law function with a power-law index of −1.7). This mission-level science requirement defines the following instrument-level requirements for the SGD:

- Effective area for the detector must be >20 cm^2 at 100 keV to obtain sufficient number of photons in a reasonable observation time (typically 100 ks).
- FOV must be <0.55 deg at 150 keV or less to minimize source confusions and the cosmic x-ray background (CXB).

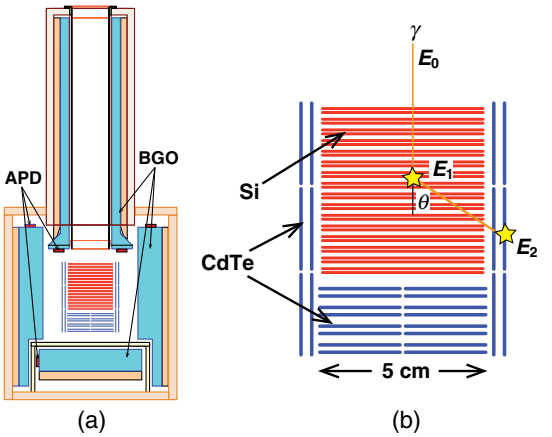

Fig. 1 (a) Schematic drawing the SGD and (b) conceptual drawing of a gamma ray interacting with a Compton camera in the SGD.

- Energy resolution [full width at half maximum (FWHM)] must be better than 2 keV at 60 keV to identify nuclear lines from activation backgrounds.

To fulfill the above requirements, the SGD design includes two identical units with each holding three Compton cameras with a geometrical area of ∼25 cm^2 surrounded by BGO active shields as shown in Fig. 1(a). The geometry of the BGO scintillator defines ∼10-deg FOV of the telescope for high-energy photons while a passive phosphor bronze collimator [called the fine collimator (FC)] restricts the FOV to ≲0.55 deg for low-energy photons (≲150 keV). Scintillation light from the BGO scintillators is detected by avalanche photodiodes (APDs), allowing a compact design as compared with phototubes.

The Compton camera is employed as a direction-sensitive gamma-ray detector. The Compton camera records the energies and locations of a recoil electron and a scattered photon in a Compton scattering, which can be utilized to constrain the direction of the incident photon using the Compton kinematics. The hybrid design of the SGD Compton camera incorporates both pixelated Si and CdTe semiconductor sensors. The Si sensors are used as the scatterer since the Compton scattering is the dominant process in Si above ∼50 keV compared with ∼300 keV for CdTe. The Si sensors also yield better constraints on the Compton kinematics because of a smaller effect from the finite momentum of the Compton-scattering electrons (so-called Doppler broadening) than CdTe (approximately by a factor of 2). The CdTe sensors are used as the absorber of the scattered gamma ray following the Compton scattering in the Si sensors, taking advantage of higher photoabsorption probability than Si. A combination of two materials with low and high Z (atomic number) is also beneficial for lowering backgrounds since neutron scattering is suppressed in high-Z materials while activation backgrounds are negligible in low-Z materials. Note that neutron and activation backgrounds are the dominant non-x-ray background contributions expected in the SGD based on the experience with the Suzaku HXD.[30]

The SGD detects gamma-ray events where a gamma ray interacts twice in the Compton camera, once by Compton scattering in a Si sensor and then by photoabsorption in a CdTe sensor. Once the locations and energies of the two interactions are

measured, as shown in Fig. 1(b), the direction of the incident photon can be determined as

$$\cos\theta = 1 + \frac{m_e c^2}{E_2 + E_1} - \frac{m_e c^2}{E_2}, \tag{1}$$

where θ is the polar angle of the Compton scattering (the angle between the incident and scattered gamma rays), and E_1 and E_2 are the energies deposited in each photon interaction. The high-energy resolution of the Si and CdTe devices is essential for reducing the uncertainty of θ. The angular resolution is limited to ~8 deg at 100 keV due to the Doppler broadening[31] and ~3 deg at 600 keV due to pixel size of the semiconductor sensor in the SGD. We require that the incident photon angle inferred from the Compton kinematics is consistent with the FOV, which dramatically reduces dominant background sources, such as radioactivation of the detector materials and neutrons. The low background realized by the Compton kinematics is the key feature of the SGD since the background is the major limiting factor of the SGD sensitivity for faint sources.

As a natural consequence of the Compton approach, the SGD is also sensitive to gamma-ray polarization,[32–34] thereby opening up a new window to probe the geometry and mechanism of gamma-ray emissions, the structure of magnetic fields in compact objects and astrophysical jets, and fundamental physics, such as vacuum birefringence effects predicted by some quantum gravity models. The Compton-scattering cross section depends on the azimuthal Compton-scattering angle with respect to the incident polarization vector as

$$\frac{\delta\sigma}{\delta\Omega} \propto \left(\frac{E'_\gamma}{E_\gamma}\right)^2 \left(\frac{E_{\gamma'}}{E_\gamma} + \frac{E_\gamma}{E'_\gamma} - 2\sin^2\theta\cdot\cos^2\phi\right), \tag{2}$$

where ϕ and θ are the azimuthal and polar angles of the Compton scattering, respectively, and E_γ and E'_γ are the incident and scattered photon energies, respectively. It indicates that the ϕ modulation is the largest at $\theta = 90$ deg, i.e., perpendicular to the incident polarization vector.

3 Instrument Design

The SGD system consists of two identical sets of SGD sensors (SGD-S), two SGD analog electronics (SGD-AEs), SGD digital processing units (SGD-DPU), and SGD digital electronics (SGD-DE) (although the two differ by the location of the radiator in the SGD-S).

The SGD-S is a detector body that contains a 3×1 array of identical Compton camera modules surrounded by BGO scintillators as shown in Fig. 2(a). Phosphor bronze passive collimators constrain the FOV of the Compton camera to 0.55 deg below ~150 keV to suppress the CXB and minimize source confusion. Two SGD-S units are mounted on opposite sides of the spacecraft to balance the load due to their large mass (~158 kg). A dedicated radiator is attached to the main bottom structure of the SGD-S holding the Compton camera to dissipate ~24.5 W of power produced by the SGD-S and keep the operating temperature at around −20°C. Two heat pipes are attached to the radiator and the SGD-S bottom structure to increase the heat conductivity within the radiator and the SGD-S bottom structure and also between them. The heaters attached to the SGD bottom structure and the radiator control the temperature. The main support structure and enclosure are made of carbon fiber reinforced plastic (CFRP) to obtain high rigidity while minimizing the mass. The surface of the enclosure is covered by a graphite sheet with thin adhesive to improve the heat conductivity so that the APD temperature is maintained within the requirement. The SGD-S is mounted to the side panel of the spacecraft via a base structure made of glass fiber reinforced plastic (GFRP) to minimize the thermal coupling between the SGD-S CRFP structure and the spacecraft since the spacecraft is relatively warm (~20°C). APD charge-sensitive amplifier (CSA) boards and high-voltage (HV) power supplies are enclosed in APD-CSA boxes, which are attached to the SGD structure via GFRP arms to avoid heat transfer to the main structure. The heat from the APD-CSA boxes is transferred to the bottom structure by aluminum plates, which also act as debris shields for cables out of the APD-CSA boxes. The SGD-S and the backside of the radiator are enclosed by multilayer insulator (MLI) sheets to minimize the effect of the heat input from radiation. Additional independent MLI panels are attached at the

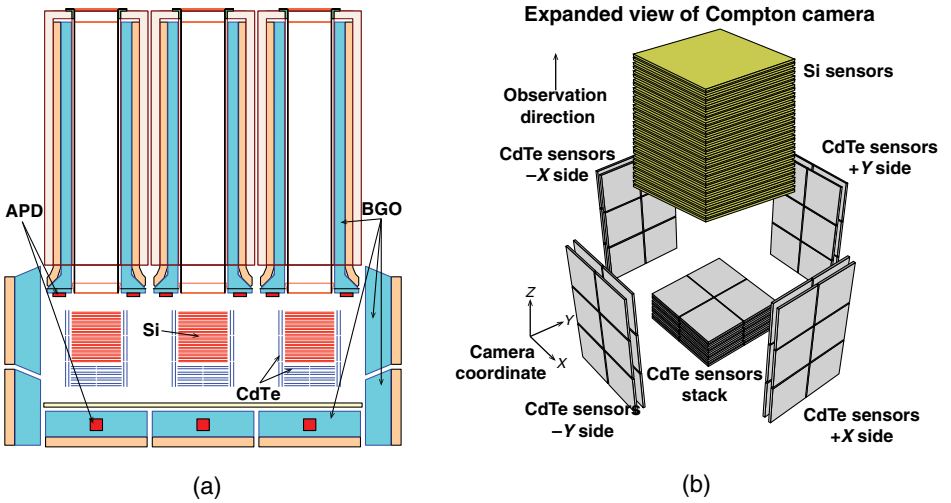

Fig. 2 Schematic drawing of (a) an SGD-S and (b) expanded view of sensor configuration of a Compton camera.

bottom to intercept solar radiation and at the satellite solar panel direction to intercept the IR emission from the solar panel. The thermal design was developed and confirmed by a thermal model with the finite-element method and some verification tests. The mechanical design was developed and confirmed by a mechanical model with the finite-element method in terms of an eigenfrequency analysis, a quasistatic load, a sine vibration, random vibration analysis, and acoustic tests. The details of the mechanical design of the SGD-S are described in Ref. 23.

The SGD-AE provides power management and housekeeping (HK) functions for the Compton camera system and the active-shield readout system. It also processes analog signals from the active-shield readout electronics. The SGD-DPU functions as a digital interface from the SGD-S and SGD-AE to the SGD-DE via the SpaceWire[35] network standard and also houses an SGD-PSU (power supply unit) inside. The SGD-DE sends commands to the SGD-DPU, performs data processing of the event and HK data, and is connected to the satellite SpaceWire network. The topology of the SpaceWire network is designed to be redundant. Data can be routed via another DPU if one of DPU-DE or DE-router connections fails. In addition, a spare DE that can be used by any instrument on the satellite is included in the payload; the data can be routed to the spare DE if one of the SGD-DEs malfunctions. Design details of each component are described below.

3.1 *Compton Camera*

Taking advantage of 15 years of development,[11–13,31,36–42] the SGD Compton camera is optimized to detect gamma rays up to 600 keV. A Compton camera consists of a stack of 32 layers of 0.6-mm-thick Si pixel sensors[43] followed by 8 layers of 0.75-mm-thick CdTe pixel sensors,[44,45] surrounded by 2 layers of 0.75-mm-thick CdTe pixel sensors on the four sides as shown in Fig. 2(b). Each Si sensor has a 16×16 array of 3.2×3.2 mm^2 pixels, and each CdTe sensor has an 8×8 array of 3.2×3.2 mm^2 pixels. Each layer of CdTe sensors in the stack is composed of 2×2 CdTe sensors to match the area of Si sensors, and each layer of CdTe sensor on the side is composed of 2×3 CdTe sensors. The pixel size is optimized to minimize the number of pixels for lower power consumption while avoiding the pixel size being the dominant contribution to the angular resolution of Compton kinematics. The thicknesses of Si and CdTe sensors are determined from constraints on the bias voltages required to operate the sensors at the best condition. The location of the CdTe sensors on the side is slightly displaced in the horizontal direction to allow placement of readout application-specific integrated circuits (ASICs) at the corner of the sensor. This arrangement allows a placement of the CdTe sensors on the side very close to the stacked Si and CdTe sensors. The average distance between stacked sensor layers is 1.8 mm, realizing a very compact scattering volume. The length and placement of the CdTe sensor on the side and the distance from the stacked sensors are determined to maximize the coverage of gamma rays scattered in the Si sensors with the minimum area of the CdTe sensors on the side.

Signals from 8×8 pixels of Si and CdTe sensors are read out by a 64-channel ASIC, VATA-SGD,[46] which can produce trigger signals, digitize pulse heights, and can be configured digitally. The signal processing chain of the Compton camera consists of 208 front-end cards (FECs) followed by four ASIC driver boards (ADBs) and an ASIC control board (ACB) as shown in Fig. 4(a). FECs are located at the four corners of the sensor modules in the sensor stack, and the backside of the CdTe sensor on the side, and have only ASICs (one ASIC for the stack module and six ASICs for the side module) and passive components, such as capacitors and miniature connectors. Five daisy chains of eight ASICs in the sensor stack are connected to one ADB, which is located on each side of the Compton camera. Two daisy chains of six ASICs in the side sensors are connected to the same ADB. Each ADB transmits digital signals between seven daisy chains of ASICs and the ACB. Only power lines and digital lines are required between ADBs and FECs, and all fast digital signals are differential to minimize the electromagnetic interference. ASICs are controlled by a field programmable gate array (FPGA) on the ACB attached at the bottom of the Compton camera. These components are packed in a $12 \times 12 \times 12$ cm^3 aluminum enclosure. Such a high-density stacking of Si and CdTe sensors is critical to obtain a high efficiency for Compton reconstruction of 10% to 15% around 100 keV. A detailed design of the SGD Compton camera is described in Ref. 41.

To suppress the leakage current of the Si, CdTe, and APD sensors and to avoid the gain variation of the APD, the temperature of the bottom structure attached to the Compton cameras and the BGO support structure needs to be kept at $-20°C \pm 5°C$ and below $-15°C \pm 5°C$, respectively, with an orbital variation of $<3°C$. The Compton camera is designed to conduct the heat of 4 W from ASICs and to keep the temperature of all sensors within 5°C of the bottom structure interface. A detailed description of thermal design of the Compton camera is given in Ref. 47.

A custom ASIC, VATA-SGD, is developed for the SGD based on the VIKING architecture,[46,48] which has been known for good noise performance and employed in various satellites, such as Swift,[49] PAMELA,[50] and AGILE.[51] In the SGD Compton camera, very little space is left for the electronics; therefore, the ASIC must integrate trigger and digitization capabilities in a single die. The VATA-SGD consists of 64 channels of CSAs with low noise [$180e^-$ (RMS) at 6 pF load] and low-power consumption ($\lesssim$0.3 mW/channel). Following each CSA, a trigger circuit is formed by a fast shaper with a peaking time of 0.6 μs and a discriminator. The CSA output is also connected to a slow shaper with a peaking time of $\sim$3 μs followed by a hold circuit so that the peak voltage can be held using the above trigger signal. The hold circuit outputs of all 64 channels are simultaneously digitized by the Wilkinson-type analog-to-digital converter where the time duration of the voltage ramp to cross the sampled voltage is measured by a counter. The conversion time is <100 μs using the external clock of 10 MHz for 10-bit digitization. The digitized data are transferred via a differential serial output. To reduce the data transfer time, the ASIC can send only the data above a certain digital value which can be adjusted for each channel. The ASIC produces all necessary analog bias currents and voltages by internal digital-to-analog converters except for the main bias current which sets the scale of all bias currents; this is provided by an external resistor on the FEC. Owing to all the functionality integrated in the ASIC, we only need an FPGA, several digital drivers and receivers, and passive components (resistors and capacitors) to operate 208 ASICs in a Compton camera. The data input and output circuits on the ASIC are designed to allow daisy chaining of multiple ASICs to reduce the number of signal paths. In the SGD Compton camera, six or eight ASICs are daisy chained.

3.2 *BGO Active Shield and Support Structure*

The thick active shield made of 25 BGO scintillators coupled with APDs is employed to reduce in-orbit background of the SGD.[52–55] The BGO crystal is dense (7.1 g/cm^3), has a high stopping power (i.e., short radiation length of 1.1 cm), high optical transparency, and ability to form a large crystal although its light output is lower than NaI or CsI.

In addition to providing anticoincidence signals for cosmic rays and gamma rays from outside of the FOV, the BGO shield is also used to reduce the number of SAA protons penetrating to the cameras since those protons are the main cause of the activation of sensor materials. The BGO shape is designed so that any trajectory that intersects with the Compton camera must go through at least 3 cm (2.7 radiation length) of BGO before it reaches the camera. We employ a modular mechanical structure for the BGO shield where each BGO crystal is supported by a CFRP base plate to make it easier to handle each BGO module. The BGO enclosure consists of a CFRP base plate that is glued to the BGO crystal via $BaSO_4$-based reflector painted on the BGO and CFRP covers. The $BaSO_4$-based reflector is chosen for the adhesive strength with modest reflectivity. The remaining sides of the BGO crystal are covered by both enhanced specular reflector and Gore-Tex sheet for better reflection properties.

The APD is chosen for the photon detector of the BGO shield mainly due to its compact size compared with photomultipliers and also due to compatibility with a modular structure of the shield. Although the larger APD yields better photon collection efficiency (nearly proportional to the root square of the area), the capacitance and the leakage current of the APD also increases proportionally to the area. Based on the experiments with 3×3, 5×5, 10×10, and 20×20 mm^2 APDs, we concluded that 10-mm size gives the best signal-to-noise ratio for our application. We employ HPK S8664-55 with slightly modified structure for less leakage current; those were used by the Compact Muon Solenoid, an experiment for the Large Hadron Collider at the European Organization for Nuclear Research. The APD is encapsulated by silicone resin rather than epoxy resin, to avoid cracks that appeared in epoxy resin due to thermal cycles.

Since the gain of the APD is temperature dependent ($-3\%/°C$), the temperature of the APD needs to be controlled within 3°C to keep the gain variation within 10%. If the temperature variation cannot be controlled within 3°C, the APD bias voltage needs to be adjusted to compensate for the gain change.

Signals from the APDs are routed to CSAs in shielded boxes located in the close vicinity of the APDs on the SGD-S enclosure. Since the APD capacitance is relatively large, ~270 pF, a low-noise CSA is developed to obtain ~1300 electrons (FWHM).

3.3 *Fine Collimator*

The BGO active shield has an opening of 9.2×9.2 deg^2 (FWHM), which is rather large, and thus would result in the CXB higher than non-x-ray backgrounds and substantial source confusions within the FOV below ~150 keV. FCs are installed in the opening of the BGO active shield, to reduce the FOV to 0.55 deg (FWHM). The collimator consists of 16×16 array of square cells with a pitch of 3.2 mm and a length of 324 mm. Each cell is divided by 0.1-mm-thick phosphor bronze (PCuSn), yielding an aperture opening of ~94%. These choices of the material and the geometry yield negligible leakage for 100 keV and 10% leakage at 150 keV and 0.55 deg from the FOV center as shown in Fig. 3. To achieve the effective area >20 cm^2 at

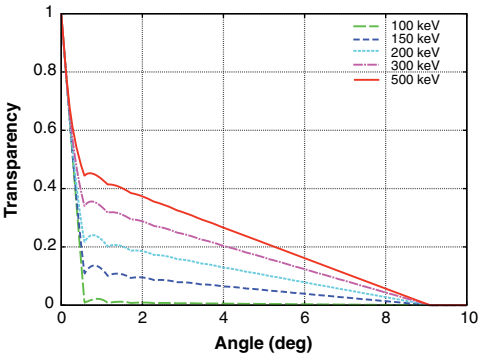

Fig. 3 Analytical calculation of the transparency of the fine collimator as a function of the angle from the FOV center.

100 keV, the loss of the effective area due to the FC aperture opening and misalignment must be <20%.[56] The effective FC aperture opening, including the effect of the imperfect shape of the FCs, is expected to be better than 90%. Misalignment of the FCs may be caused by misalignment among six collimators, thermal distortion of the SGD-S structure, and misalignment of the SGD-S with respect to the satellite optical axis. The total misalignment should be below 3.3 arc min to keep the total loss below 20%.

3.4 *Electronics*

The SGD electronics system consists of two processing chains, one for Compton cameras and the other for APDs as shown in an SGD electronics block diagram in Fig. 4(b). The Compton camera electronics system includes three Compton cameras, two camera HV power supplies, two DC/DC converters, a camera power management unit (CPMU), and a mission I/O (MIO) board. The CPMU controls power supplies (both HV power supplies and DC/DC converters) and HV levels, and monitors power supply voltages and currents, and temperatures around cameras. HV power supplies are controlled via slow serial data link and have low-pass filters to avoid a sudden change of the HV output. The MIO board sends control signals to the camera and receives the data from the camera via low-voltage differential signaling (LVDS). The MIO board also formats the camera data, controls the CPMU, and communicates with the SGD-DE via SpaceWire network interface.

The APD electronics system includes 25 APDs, 25 APD-CSAs, four APD HV power supplies, two APD processing and management units (APMUs), and an MIO board. The APMU receives APD signals from APD-CSAs and continuously digitizes them with flash ADCs. The FPGA on the APMU immediately applies a digital filter on the digitized APD signal and issues anticoincidence signals with three threshold levels: the lowest possible threshold to detect any particle that deposits energy in the BGO, a threshold to detect minimum ionizing particles, and a threshold to detect iron nuclei. We have two digital filters for the lowest possible threshold to provide a fast anticoincidence to abort the data acquisition in progress and a slow anticoincidence for offline analyses with a better energy resolution. Other APMU functions include creating pulse height histograms, detection of transient events in BGOs, control of power supplies and their voltages, and monitoring of power supply voltages and temperature around APDs. The MIO board sends control signals to and receives digital data from the APMUs via LVDS.

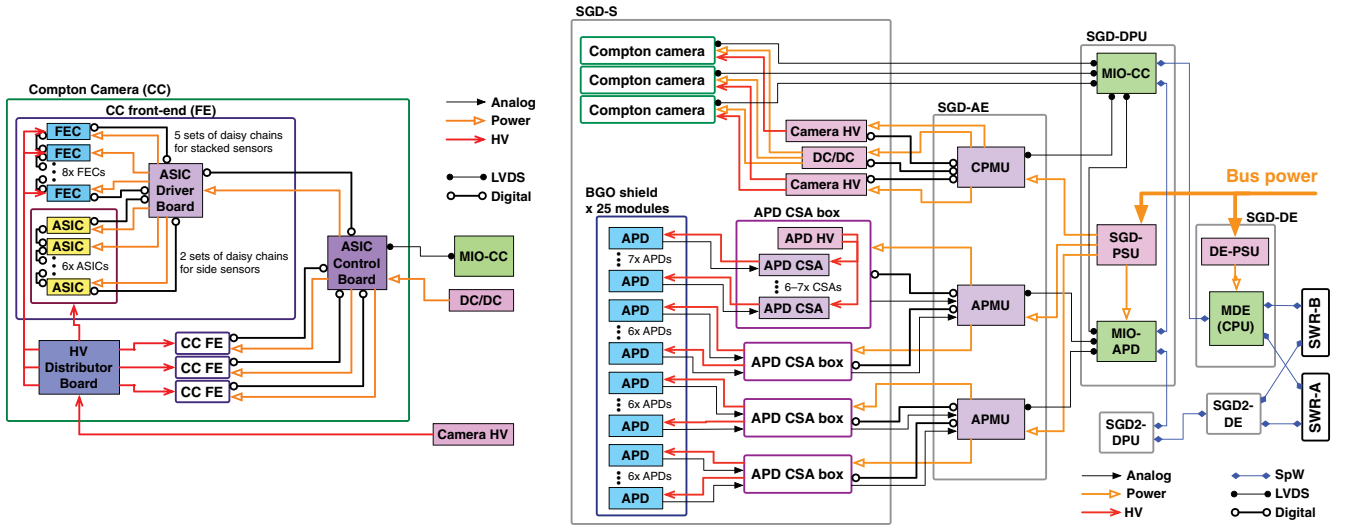

Fig. 4 Block diagram of (a) the Compton camera electronics systems and (b) the SGD electronics system.

3.5 *Data Acquisition System*

The data acquisition of the Compton camera in the SGD is initiated by the primitive trigger issued from any ASIC. The primitive triggers from all ASICs in a Compton camera are processed by the ACB in the Compton camera. The ACB checks the coincidence pattern of those primitive triggers for any sign of charged-particle tracks that tend to produce triggers in many consecutive layers. The coincidence time is 0.4 μs. If ACB does not find any sign of the charged-particle tracks, it sends the trigger signal to the MIO board. The MIO board sends back trigger acknowledgment to the ACB if no other Compton camera is in the data acquisition phase. Since the data acquisition activities in one Compton camera affect the trigger performance of the other Compton cameras in the same SGD-S, we do not accept new triggers during the data acquisition. Upon reception of the trigger acknowledgment from the MIO board, the ACB sends hold signal to all ASICs in the Compton camera with appropriate delay ($\sim$3 μs) so that the slow shaper signal of the ASIC can be sampled near the peak of the pulse shape and activate the digitization mode. While we wait for the ASIC to stabilize after the digitization mode is activated, the MIO board checks the output of the fast anticoincidence signals from the BGO system. If any anticoincidence signal is issued within 6 μs of the activation of the digitization mode, the data acquisition is aborted before the actual digitization is started to minimize the dead time. Unless the abort signal is issued by the MIO board within 6 μs from the trigger acknowledgment, the ACB activates the digitization sequence of all ASICs in the Compton camera. This BGO anticoincidence functionality was not activated during the verification phase of the satellite operation. In addition, slow anticoincidence signals from the BGO system, with lower energy threshold for better performance, were also recorded for offline analyses. A detailed description of the Compton camera data acquisition is given in Ref. 41.

The BGO data acquisition operates independently of the Compton camera. The FPGA on the APMU continuously process the BGO signal and sends anticoincidence signals to the MIO board whenever it detects signals above thresholds. It also produces histograms of the peak energies at a certain interval. Those histograms are used for gain calibrations of each BGO module. Gamma-ray bursts may be detected if it finds a sudden increase of the anticoincidence rates. A detailed description of the BGO signal processing is given in Ref. 55.

The SGD data mainly consist of the event and HK data. The event data include the absolute time, the time after previous trigger, raw ASIC data, and various flags, including anticoincidence flags from BGOs. The HK data include time, temperatures, power supply status, and measured voltages of the power supplies.

4 Verification Tests on Ground

Thermal and mechanical models of the SGD-S were fabricated to verify those performances of the structure. An engineering model of the Compton camera was fabricated to verify the functionality, thermal, mechanical, and electric performance of the Compton camera. The flight hardware fabrications were completed on November 2014 for SGD1 and on January 2015 for SGD2. The pictures of the SGD1-S and SGD2-S with their radiators are shown in Fig. 5(a). The pictures of the SGD1-S and SGD2-S attached to the satellite are shown in Figs. 5(b) and 5(c), respectively.

Performance verification tests and environmental tests were conducted from November 2014 until March 2015. Performance verification and calibration tests were carried out in a large thermostatic chamber at ISAS/JAXA. The SGD-S and SGD-AE were operated at a temperature of -27°C. Gamma-ray data from the radioisotopes and test pulse calibration data of the Compton cameras were obtained at the nominal operating temperature of the SGD-S. Thermal vacuum tests of the SGD subsystem were conducted for the final confirmation of the thermal performance of the fabricated hardware in the 8-m space chamber at Tsukuba Space Center of JAXA. In-orbit environment was simulated using liquid N_2 shroud. The SGD-S, including the radiator, the heat pipes, the MLIs, and the HV power supplies for the detectors, the SGD-AE, and the SGD-DPU worked properly in the thermal vacuum environment simulating

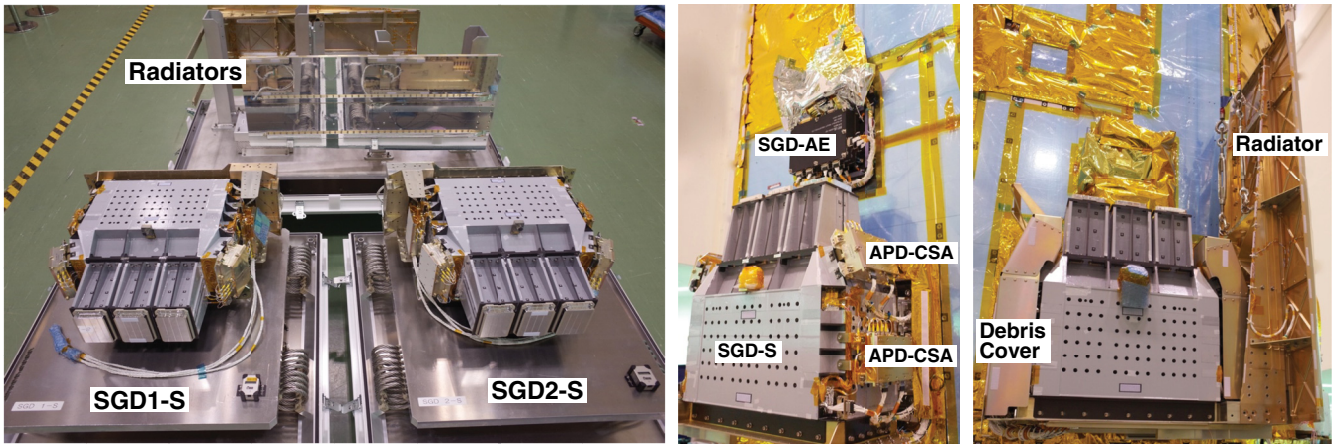

Fig. 5 Picture of (a) the SGD1-S and SGD2-S with their radiators, (b) the SGD1-S and SGD1-AE attached to the satellite, and (c) the SGD2-S and SGD2-AE attached to the satellite. CSA-boxes on the side of the SGD2-S are covered by the aluminum debris shields. The SGD2-AE is covered by the MLI sheets.

the in-orbit conditions, and the thermal design of the SGD subsystem was verified. Moreover, long-term test data of on-ground backgrounds were obtained.

Vibration tests and acoustic tests were conducted as mechanical acceptance tests at Tsukuba Space Center. No damage was seen in the functional checks before and after those tests.

After the SGD systems were attached to the satellite in April 2015, the satellite environmental tests were conducted from June 22, 2015, until October 13, 2015. In these tests, the SGD successfully maintained its operating temperature in an environment very close to the orbit. Additionally, on-ground background data were also collected at the operating temperature.

5 SGD Operations in Orbit

Hitomi was launched on February 17, 2016. The altitude and the inclination with respect to the Earth equator are 575 km and 31 deg, respectively. Commissioning of the SGD started with the power-on operation on March 1, 2016. After turning on the power for the SGD-DE, SGD-DPU, and SGD-AE, we started monitoring the HK telemetries of the SGD, including temperatures. The SGD-S was gradually cooled down to −25°C from March 3 until March 13 by adjusting the SGD heater settings.

Start-up operation of the SGD-S began from March 15, 2016. First, the Compton cameras, APD-CSA, and HV modules for Compton cameras and APDs were powered on, and then we gradually raised the HV and got detectors into the nominal observation mode. The SGD1-S was in the nominal observation mode from March 21 and operational for the observations of the supernova remnant G21.5–0.9, the neutron star RX J1856.5–3754, and the Crab Nebula. The SGD2-S was in the nominal observation mode from March 24 and operational for the observations of RX J1856.5–3754 and the Crab Nebula.

The exposure of the Crab observation was about 5 ks; however, the CdTe HV for two Compton cameras in SGD2 was turned off, because one channel in the CdTe sensors in one of the Compton cameras became noisy. (Two cameras were turned off since they share the same HV power supply.) Therefore, only Si sensor signals were taken from these two Compton cameras during the Crab observation.

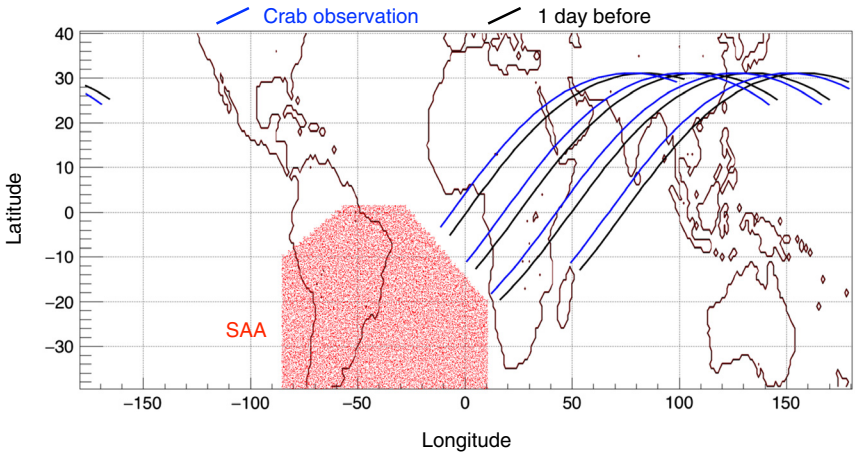

Fig. 6 Satellite position during the Crab observation (blue line) and one day before the Crab observation (black line). The red region corresponds to the SAA.

The data before the maneuver to the Crab Nebula can be used for background studies of the SGD because G21.5–0.9 and RX J1856.5–3754 are faint in the SGD energy band. Figure 6 shows the satellite position before and during the Crab observation. The satellite positions one day before and during the Crab observation are shown in the black and blue lines, respectively. The background data taken one day before the Crab observation can be used to estimate the background rates and spectra since the satellite's orbital positions are very close to those for the Crab observations. The Crab observation on March 25 started soon after the passage of the SAA shown as the red region in the figure. Therefore, the background rates during the Crab observation are high.

6 Performance

6.1 *BGO Shield Performance*

All of the 50 BGO shield modules in the SGD1-S and SGD2-S worked stably in orbit. Figure 7(a) shows spectra for a BGO module with different observing orbits divided by SAA passages. The 511-keV annihilation line and other gamma-ray lines from radioactivation of detector materials apparent in this figure can be used to derive the energy scale and the threshold energy of the BGO signals. The stability of the energy scale is also confirmed to be within 10% by monitoring the peak position of the 511-keV line. Figure 7(b) compares the distributions of the lowest threshold energies with the slow filter of all BGO shield modules obtained on ground (black) and in orbit (red). Note that the on-ground performance is slightly different from that in Ref. 55 since it derived the results from different on-ground tests. The in-orbit data show slightly better thresholds presumably due to the lower operating temperature, which indicate the anticoincidence performance of the BGO shield is not worse than that verified on ground.

Figure 7(c) shows the BGO count rates for the lowest threshold with the slow filter as a function of time in one day for the average rate (black curve), and the BGO modules with highest rate (red curve) and lowest rate (blue curve). Background variations due to the varying cutoff rigidity (COR) of cosmic rays and the SAA passages can be seen. The BGO shields operated properly even during SAA passages and the sharp increases of the count rates were as expected. Outside of the SAA passages, gradual modulations of the count rate are found to be well anticorrelated with the COR values. The average count rates vary by module and ranges from 0.5 to 1.8 kHz per module, which is consistent with our expectation of 0.5 to 2.1 kHz based on the Suzaku HXD BGO data.

The SGD BGO system is very massive and good at detecting gamma rays and measuring spectra from transient events, such as gamma-ray bursts and terrestrial gamma-ray flashes. There was no autodetection of transient events during the SGD operation period since its search parameters had not been adjusted on orbit. However, we found a candidate for a gamma-ray burst (GRB) by manually searching for transient events. This GRB was found to be GRB 160324A. The top panel of Fig. 8(a) shows the count rate of some SGD BGOs as a function of the time since 15:58:34 UT (this is the trigger timing by INTEGRAL SPI-ACS), where clear increase of the count rate is observed. The middle and bottom panels of Fig. 8(a) also show the count rates of INTEGRAL SPI-ACS and Konus-Wind. This event could have been autodetected if the proper search parameters had been in place. Figure 8(b) shows the energy spectrum observed by the SGD BGOs in the 30-s period indicated in Fig. 8(a). The background spectra are estimated by a linear interpolation of the 30-s period before and after the burst and subtracted from the observed spectra. A fit to a power-law function yields a power-law index of $-3.03^{+0.28}_{-0.31}$ and a fluence of 1.38×10^{-5} erg/cm in the 100- to 1000-keV band. Here, the effective area is obtained from the MC simulation that was verified by the calibration tests with various source directions on ground. These results for spectral parameters are within the expected ranges found in typical gamma-ray bursts.

6.2 *Fine Collimator Alignments*

The alignment of each FC was adjusted after they were installed. As a result, the viewing axis of the FC was aligned within 1.5 arc min of the nominal viewing axis of the SGD-S (an average misalignment was 0.8 arc min). This is much smaller than the FC alignment requirement of 3.3 arc min to accommodate remaining misalignment factors, such as thermal distortion of the SGD-S structure and misalignment of the SGD-S with respect to the satellite optical axis.

We checked the count rate of each Compton camera during the Crab observation since misalignment among the FCs would appear as a dispersion of the count rates among Compton cameras. The thickness dispersion of the active and inactive layers of Si sensors would affect the count rates; however, those effects

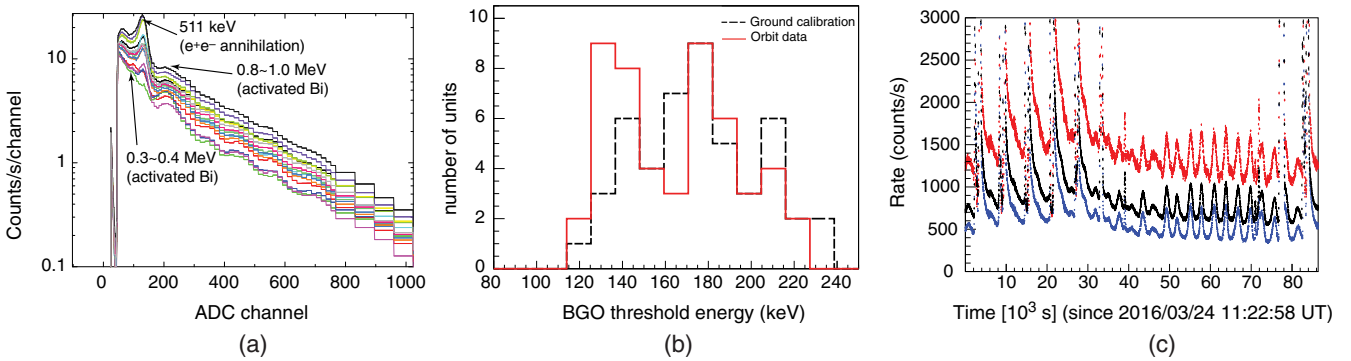

Fig. 7 (a) Spectra for a BGO module with different observing orbits divided by SAA passages. (b) Comparisons of the distributions for the BGO threshold energies obtained on ground (black dashed) and in orbit (red solid). (c) BGO count rates as a function of time for the average rate (black curve), and the BGO modules with highest rate (red curve) and lowest rate (blue curve). The data were taken from 18:00 UTC on March 23 till 18:00 on March 24.

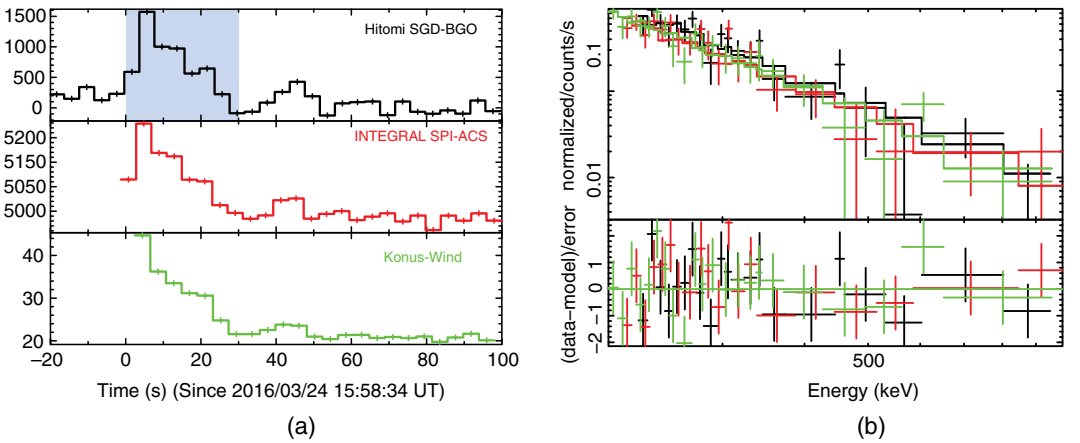

Fig. 8 (a) Count rate as a function of the time for some SGD BGOs (top), INTEGRAL SPI-ACS (middle), and Konus-Wind (bottom). Time for Konus-Wind was adjusted by 0.6915 s with respect to that for SPI-ACS to account for the arrival time difference due to the different satellite locations. A clear increase of the count rate is observed in the SGD BGOs. The hatched region in the top panel indicates the time period used for following spectral analysis. (b) Energy spectrum observed by three SGD BGOs with the most count increases. Three different colors indicate the spectra of three BGOs.

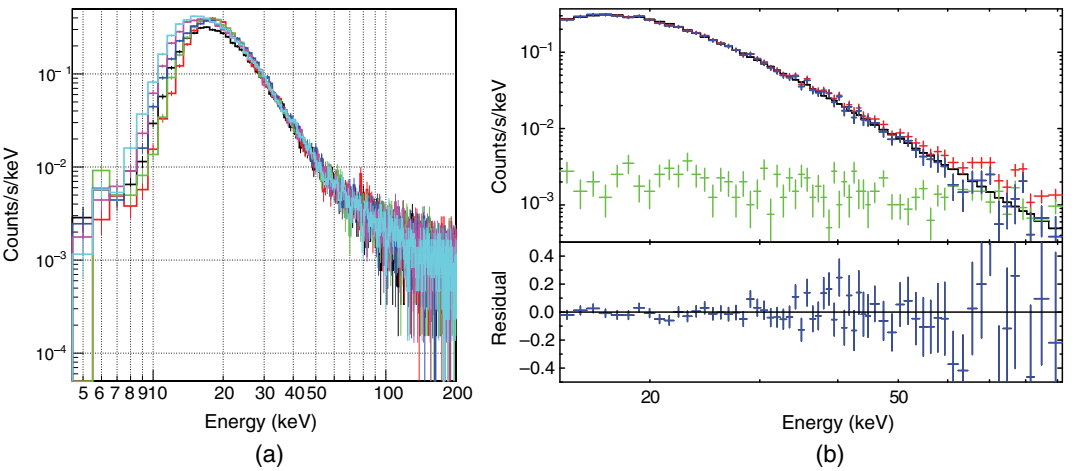

Fig. 9 (a) Spectra for all pixels in the top four layers of Si sensors where most hits are due to photoabsorption of the low-energy gamma rays. Different colors show spectra for different Compton cameras. (b) Observed spectrum for all pixels in the top four layers of the Si sensors of the Compton camera 1 in the SGD1 (red), the background spectrum taken one day before the Crab observation (green), the observed spectrum with the background subtraction (blue), and the simulation spectrum (black). The simulation assumes a power-law spectrum with a power-law index of −2.11.[57] The lower panel shows the residual [(observed counts) − (background) − (simulation)]/(simulation), as a function of the energy.

are expected to be much smaller than the FC misalignment effect. Figure 9(a) shows the spectra for all pixels in the top four layers of Si sensors without anticoincidence signals in the active shield where most hits are due to photoabsorption of the low-energy gamma rays. (Hereafter, we always require the absence of any anticoincidence signals in the active shield for the analysis of the Compton camera data.) Different colors show spectra for different Compton cameras. Since we have not adjusted the thresholds of each channel, the spectra below 30 keV are not consistent. The count rates in the energy range, 35 to 60 keV, where the effects of threshold dispersions and background subtraction are negligible, are listed in Table 1. The count rates agree with each other within 3% among the six Compton cameras. This corresponds to <1.0 arc min of misalignments among six FCs, which is consistent with the average misalignment of 0.8 arc min.

To confirm the alignment with the optical axis of the satellite, we compared the observed rate for the Crab Nebula with that from the Monte Carlo simulation assuming the nominal Crab flux. Figure 9(b) shows the observed spectrum of the Compton camera 1 in the SGD1 (red), the background spectrum taken one day before the Crab observation (green), the observed spectrum with the background subtraction (blue), and the simulation spectrum (black). In the simulation of the Crab Nebula observation, we assumed a power-law spectrum, $N \cdot E^{-\Gamma}$, with $\Gamma = 2.11$.[57] By scaling the integrated rate of the simulated spectrum in the 25- to 60-keV range to match the observed rate, we obtain $N = 8.97 \pm 0.21$ (statistical error only), which corresponds to a flux of $(8.28 \pm 0.20) \times 10^{-9}$ erg/cm^2/s^2 in the 25- to 60-keV range. Here, the energy range is extended to 25 keV since the simulation accounts for the threshold effects. A recent measurement of the absolute flux for the Crab Nebula

Table 1 Count rates of top four layer of Si sensors for six Compton cameras during the Crab observation.

	Count rates in 35–60 keV (c/s)	Deviation from the average (%)
SGD1 Compton camera 1	0.471 ± 0.012	-3.2 ± 2.6
SGD1 Compton camera 2	0.479 ± 0.013	-1.4 ± 2.7
SGD1 Compton camera 3	0.493 ± 0.013	$+1.5 \pm 2.6$
SGD2 Compton camera 1	0.500 ± 0.012	$+2.9 \pm 2.5$
SGD2 Compton camera 2	0.483 ± 0.011	-0.7 ± 2.4
SGD2 Compton camera 3	0.490 ± 0.012	$+0.8 \pm 2.4$
Average	0.486 ± 0.005	—

by NuSTAR (observations were done in October 2015 and April 2016) gives $\Gamma = 2.106 \pm 0.006$, $N = 9.71 \pm 0.16$,[57] which corresponds to a flux of $(9.25 \pm 0.05) \times 10^{-9}$ erg/cm^2/s in the 25- to 60-keV range (a correlation between N and Γ is taken into account). The Crab flux observed by the SGD is ∼10% lower than that by NuSTAR, which is not inconsistent with the expected losses of 7% for the effective area due to known misalignment and distortion of the FCs, considering that we still have unknown misalignment effects, such as the thermal distortion of the SGD-S structure and misalignment of the SGD-S with respect to the satellite optical axis. (The satellite operation was terminated before we had opportunities to measure those remaining misalignment effects.)

6.3 *Noise Performance of Compton Camera*

Noise performance and energy resolution of the Si and CdTe sensors in the Compton camera are critical to reject backgrounds from nuclear emission lines and to reject continuum

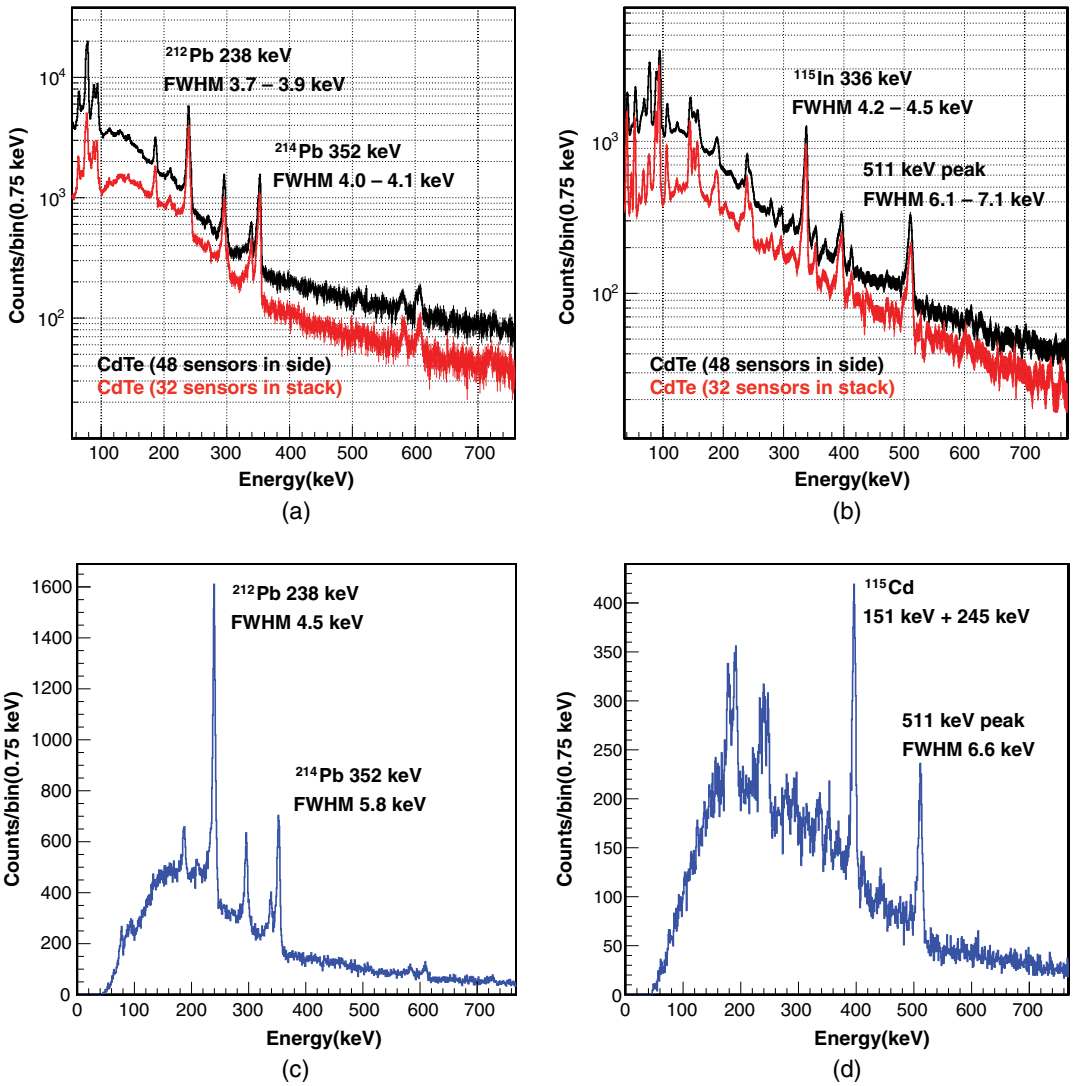

Fig. 10 (a) Single-hit spectra of CdTe sensors in a Compton camera taken on ground. The spectrum of all channels in 48 CdTe sensors on the side and that of all channels in 32 CdTe sensors in the stack are shown in black and red, respectively. (b) Single-hit spectra of CdTe sensors on the side (black) and in the stack (red) taken in orbit. (c) Spectrum for Compton events in a Compton camera taken on ground. (d) Spectrum for Compton events in a Compton camera taken in orbit.

backgrounds by Compton kinematics with high efficiencies. The energy resolution of the sensors was verified by the width of nuclear emission lines observed by the Compton cameras before and after the launch.

Figure 10 shows single-hit spectra of CdTe sensors in a Compton camera and a spectrum for Compton events[42] obtained during the thermal vacuum test of the satellite and corresponding spectra in orbit. Compton events are double-hit events, in which the energy values of two hits are consistent with a Compton scattering followed by a photoabsorption. (Consistency between the inferred direction of the incident photon and the FOV is not required at this point.) Nuclear emission lines from naturally occurring radioisotopes are clearly detected in the spectra taken on ground. In-orbit, nuclear emission lines from activated materials are observed. For example, the lines around 192, 247, 336, 392, and 396 keV are considered to originate from activated cadmium. The 396-keV line is more prominent in Compton events since it is actually a sum of 151- and 245-keV lines from ^{111}Cd. The Compton kinematics constraints reduce this line; however, some of them still remain. The energy resolutions obtained from the fit differ between the CdTe sensors in the stack and in the side. The spectra for the CdTe sensors in the side suffer more backgrounds from the surrounding material. Because of this, the peak fit may include more tail components for the CdTe sensors in the side.

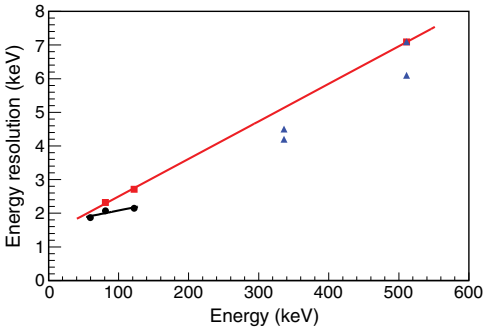

Fig. 11 Energy resolution (FWHM) of single hits as a function of the line energies for Si and CdTe sensors. Black (circle) and red (square) points indicate the energy resolutions for Si and CdTe sensors on ground, respectively. Black and red lines show fits to a linear function for black and red points, respectively. Blue (triangle) points show the energy resolutions for CdTe sensors in orbit.

Figure 11 summarizes the energy resolution of single hits as a function of the line energies for Si and CdTe sensors. Black and red points indicate the energy resolutions for Si and CdTe sensors on ground, respectively. Blue points show the energy resolutions for CdTe sensors in orbit. Two points for each energy show the energy resolution in the stack (better resolution) and in the side. The energy resolution in orbit is slightly better than the performance observed on ground due to lower operating temperature in orbit, and no degradation was observed from the performance obtained in the component level tests.[23,24,41]

6.4 *Compton Reconstruction Performance*

Rejection of backgrounds coming from outside of the FOV is the most crucial capability for the SGD. We verified the background rejection capability using the data observed before the maneuver to the Crab Nebula.

Figure 12(a) shows the light curve of Compton events in a Compton camera of the SGD1. The energy range is from 50 to 600 keV, and no event selection based on the Compton-scattering angle is applied. The gaps in the light curve correspond to SAA passages (where the data acquisition is disabled). The background count rate increases soon after the SAA passages and decreases after the SAA. The background variation is produced by radiations from activated material due to SAA protons.

Figure 12(b) shows the background spectra of Compton events in the same Compton camera after the event selection on the Compton-scattering angle. The background spectrum from orbits right after the SAA passages [corresponding to the red hatched period in Fig. 12(a)] is shown in red, and the spectrum from orbits without SAA passages [corresponding to the green hatched period in Fig. 12(a)] is shown in green. For comparisons, the background spectrum on ground is shown in black. The difference between the red and green spectra is due to radiations from short-lived isotopes activated by the SAA, including the 511-keV line and other nuclear emission

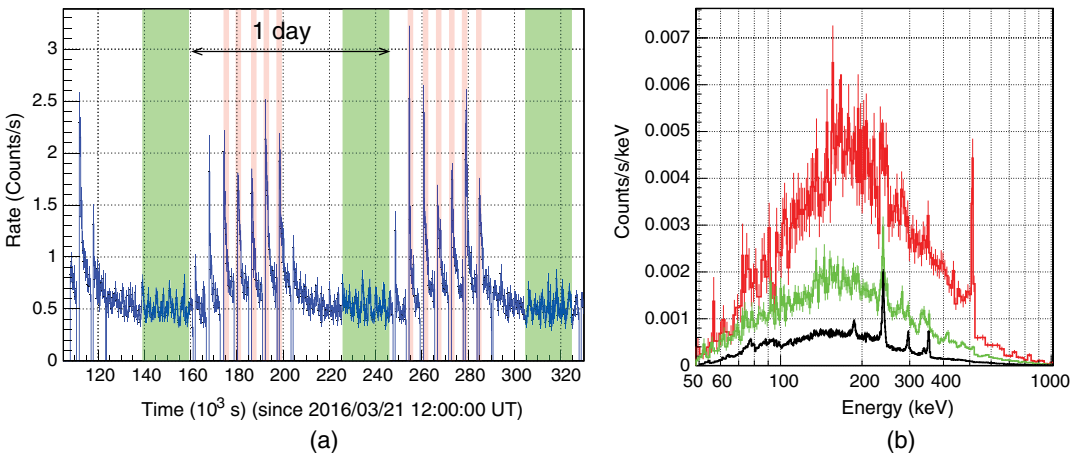

Fig. 12 (a) Light curve of Compton events in 50 to 600 keV from a Compton camera of the SGD1. (b) The background spectra obtained on the above Compton camera. The red histogram shows the background spectrum from orbits after SAA passages, corresponding to the red periods in (a), and the green histogram shows the spectrum from orbits without SAA passages, corresponding to the green periods in (a). The black histogram shows the on-ground background spectrum obtained in the thermal vacuum test of the Hitomi satellite.

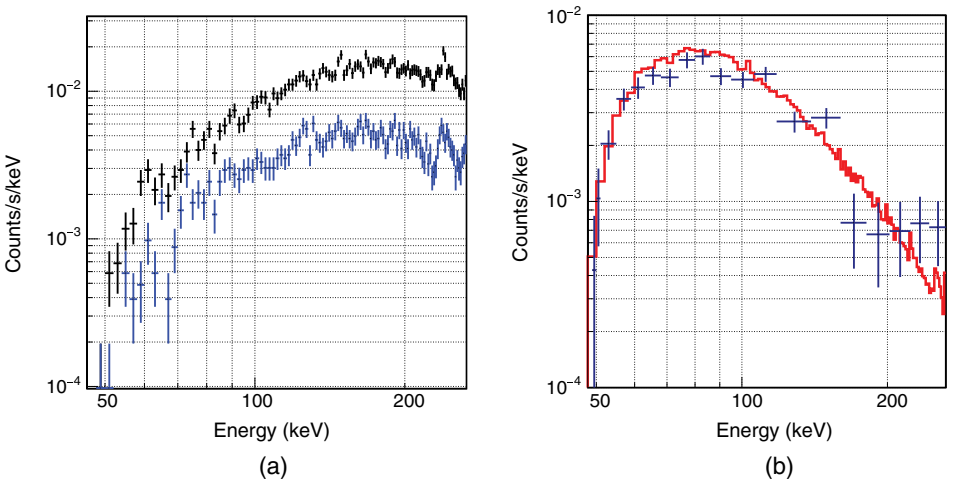

Fig. 13 (a) Spectra for the background in orbit before (black) and after (blue) the event selection on the Compton kinematics. (b) Spectrum of events which pass Compton reconstruction criteria for the data taken during the Crab observation. The background is subtracted. The events from four Compton cameras (excluding two Compton cameras, which were turned off during the Crab observation) are summed. The spectrum of the Monte Carlo simulation is shown in red.

lines. The difference between the green and black spectra is due to radiation from long-lived isotopes activated by the SAA, and those would accumulate over time until an equilibrium is reached of isotope production and decay.

Figure 13(a) compares spectra for the background in orbit before (black) and after (blue) the event selection based on the constraint on the scattering angle between the FOV and scattered photon direction as described in Ref. 42. With this selection, the background rate is reduced by a factor of 3 in 100 to 200 keV. This rejection factor appears small because the majority of non-gamma-ray backgrounds and partial events where photoabsorption takes place outside of the Compton camera are rejected due to nonphysical scattering angle calculated from energies, and also gamma-ray backgrounds from the outside of the FOV may still satisfy the constraint on the scattering angle between the FOV and scattered photon direction by chance. This event selection is not optimized for the observed backgrounds and further optimization is on going for the scientific analysis of the Crab Nebula. Figure 13(b) shows the resulting spectrum of four operational Compton cameras for the Crab observation after the background subtraction. The background spectrum was estimated using the observation data 1 day earlier. The total observation time is 5167 seconds after a dead-time correction. Figure 13(b) also shows the spectrum estimated by the Monte Carlo simulation using the same event reconstruction and selection as the observation. In this simulation, we assume the same spectral function for the Crab Nebula as Fig. 9(b). The observed data and the simulation agree with each other above 100 keV, and the observed data are slightly below the simulation in 60- to 100-keV range.

The analysis of the gamma-ray polarization from the Crab Nebula is ongoing, and the result will be published in a separate paper.

7 Summary

The SGD was the Hitomi instrument that operated in the highest energy band (60 to 600 keV). Taking advantage of 15 years of development, a multilayer semiconductor Compton camera was developed for the SGD. The SGD flight hardware was fabricated and subjected to subsystem tests and satellite system tests in 2015, and the satellite was successfully launched on February 17, 2016. After the successful commissioning, the SGD started nominal observations on March 24, 2016. The energy resolution of the SGD in orbit was similar or better than that on ground. The SGD observed the Crab Nebula for approximately a half day before the spacecraft ceased to function on March 26, 2016. This makes the Hitomi SGD the second operational Compton camera in orbit since COMPTEL[58] onboard the Compton Gamma-ray Observatory[59] in the 1990s, and the first semiconductor Compton camera in orbit. Although the size of the SGD Compton camera is much smaller than COMPTEL, the SGD effective area of $\sim$20 cm^2 at 100 keV is comparable to that for COMPTEL, $\sim$40 cm^2 at 5 MeV, due to highly efficient design of the SGD Compton camera. In addition, by combining the imaging capability of the Compton camera and the narrow FOV defined by the active shield, the SGD demonstrated the reduction of the activation background by a factor of 3 in orbit.

Acknowledgments

We greatly appreciate the dedicated work by all students in participating institutions. We thank all the JAXA members who have contributed to the Hitomi (ASTRO-H) project. We acknowledge support from JSPS/MEXT KAKENHI Grant Nos. 16J02333, 24105007, 24244014, 25287059, and 26800160 and the JSPS Core-to-Core Program. All U.S. members gratefully acknowledge support through the NASA Science Mission Directorate. Stanford and SLAC members acknowledge support via DoE contract to SLAC National Accelerator Laboratory DE-AC3-76SF00515 and NASA Grant No. NNX15AM19G. Part of this work was performed under the auspices of the U.S. DoE by LLNL under Contract No. DE-AC52-07NA27344 and also supported by NASA grants to LLNL. Support from the European Space Agency is gratefully acknowledged. French members acknowledge support from the Centre National d'Études Spatiales. We thank contributions by many companies, including in particular, Mitsubishi Heavy Industries, NEC, Hamamatsu Photonics, Acrorad, Ideas, SUPER RESIN, and OKEN.

References

1. T. Takahashi et al., "The NeXT X-ray Mission," *Proc. SPIE* **7011**, 70110O (2008).
2. T. Takahashi et al., "The ASTRO-H mission," *Proc. SPIE* **7732**, 77320Z (2010).
3. T. Takahashi et al., "The ASTRO-H X-ray observatory," *Proc. SPIE* **8443**, 84431Z (2012).
4. T. Takahashi et al., "The ASTRO-H X-ray astronomy satellite," *Proc. SPIE* **9144**, 914425 (2014).
5. T. Takahashi et al., "The ASTRO-H (Hitomi) x-ray astronomy satellite," *Proc. SPIE* **9905**, 99050U (2016).
6. T. Takahashi et al., "The Hitomi (ASTRO-H) X-ray astronomy satellite," *J. Astron. Telesc. Instrum. Syst.* **4**(2), 021402 (2018).
7. P. J. Serlemitsos et al., "Design and fabrication of ASTRO-H (Hitomi) soft X-ray telescope—aluminum foil X-ray mirror," *J. Astron. Telesc. Instrum. Syst.* (2018), in preparation.
8. R. K. Kelley et al., "The astro-H high resolution soft X-ray spectrometer," *J. Astron. Telesc. Instrum. Syst.* **4**(2) (2018), in preparation.
9. T. Tanaka et al., "The soft X-ray imager (SXI) aboard the Hitomi satellite," *J. Astron. Telesc. Instrum. Syst.* **4**(1), 011211 (2018).
10. H. Matsumoto et al., "In-orbit performance of the hard X-ray telescope (HXT) on board Hitomi," *J. Astron. Telesc. Instrum. Syst.* **4**(1), 011212 (2018).
11. T. Takahashi, T. Kamae, and K. Makishima, "Future hard X-ray and gamma-ray observations," in *New Century of X-ray Astronomy, ASP (Astronomical Society of the Pacific Conference Series)*, Vol. 251, pp. 210–213 (2002).
12. T. Takahashi et al., "High resolution CdTe detectors for the next generation multi-Compton gamma-ray telescope," *Proc. SPIE* **4851**, 1228–1235 (2002).
13. T. Takahashi et al., "Hard X-ray and gamma-ray detectors for the NeXT mission," *New Astro. Rev.* **48**, 269–273 (2004).
14. T. Takahashi et al., "Wide band X-ray imager (WXI) and soft gamma-ray detector (SGD) for the NeXT mission," *Proc. SPIE* **5488**, 549–560 (2004).
15. M. Kokubun et al., "Hard X-ray imager (HXI) for the NeXT mission," *Proc. SPIE* **7011**, 70110R (2008).
16. M. Kokubun et al., "Hard x-ray imager (HXI) for the ASTRO-H mission," *Proc. SPIE* **7732**, 773215 (2010).
17. M. Kokubun et al., "The hard X-ray imager (HXI) for the ASTRO-H mission," *Proc. SPIE* **8443**, 844325 (2012).
18. G. Sato et al., "The hard X-ray imager (HXI) for the ASTRO-H mission," *Proc. SPIE* **9144**, 914427 (2014).
19. K. Nakazawa et al., "The hard x-ray imager (HXI) onboard ASTRO-H," *Proc. SPIE* **9905**, 990511 (2016).
20. K. Nakazawa et al., "The hard X-ray imager (HXI) onboard ASTRO-H," *J. Astron. Telesc. Instrum. Syst.* **4**(2), 021410 (2018).
21. H. Tajima et al., "Design and performance of the soft gamma-ray detector for the NeXT mission," *IEEE Trans. Nucl. Sci.* **52**, 2749–2757 (2005).
22. H. Tajima et al., "Soft gamma-ray detector for the ASTRO-H mission," *Proc. SPIE* **7732**, 773216 (2010).
23. S. Watanabe et al., "Soft gamma-ray detector for the ASTRO-H mission," *Proc. SPIE* **8443**, 844326 (2012).
24. Y. Fukazawa et al., "Soft gamma-ray detector (SGD) onboard the ASTRO-H mission," *Proc. SPIE* **9144**, 91442C (2014).
25. S. Watanabe et al., "The soft gamma-ray detector (SGD) onboard ASTRO-H," *Proc. SPIE* **9905**, 990513 (2016).
26. T. Kamae et al., "Astro-E hard X-ray detector," *Proc. SPIE* **2806**, 314–328 (1996).
27. T. Takahashi et al., "Hard X-ray detector (HXD) on board Suzaku," *Publ. Astro. Soc. Jpn.* **59**, S35 (2007).
28. M. Kokubun et al., "In-orbit performance of the hard X-ray detector (HXD) on board Suzaku," *Publ. Astro. Soc. Jpn.* **59**, S53 (2007).
29. Y. Fukazawa et al., "Modeling and reproducibility of Suzaku HXD PIN/GSO background," *Publ. Astro. Soc. Jpn.* **61**, S17 (2009).
30. M. Kokubun et al., "Activation of the Astro-E hard X-ray detector in low earth orbit," *IEEE Trans. Nucl. Sci.* **46**, 371–376 (1999).
31. S. Watanabe et al., "A Si/CdTe semiconductor Compton camera," *IEEE Trans. Nucl. Sci.* **52**, 2045–2051 (2005).
32. H. Tajima et al., "Gamma-ray polarimetry with Compton telescope," *Proc. SPIE* **5488**, 561–571 (2004).
33. S. Takeda et al., "Polarimetric performance of Si/CdTe semiconductor Compton camera," *Nucl. Instrum. Methods A* **622**, 619–627 (2010).
34. J. Katsuta et al., "Study of the polarimetric performance of a Si/CdTe semiconductor Compton camera for the Hitomi satellite," *Nucl. Instrum. Methods A* **840**, 51–58 (2016).
35. S. M. Parkes and P. Armbruster, "Spacewire: a spacecraft onboard network for real-time communications," in *14th IEEE-NPSS Real Time Conf.*, Vol. 5488, pp. 6–10 (2005).
36. H. Tajima, "Gamma-ray polarimetry," *Nucl. Instrum. Methods A* **511**, 287–290 (2003).
37. T. Tanaka et al., "Development of Si/CdTe semiconductor Compton telescope," *Proc. SPIE* **5501**, 229–240 (2004).
38. H. Odaka et al., "Performance study of Si/CdTe semiconductor Compton telescopes with Monte Carlo simulation," *Nucl. Instrum. Methods A* **579**, 878–885 (2007).
39. S. Takeda et al., "Experimental results of the gamma-ray imaging capability with a Si/CdTe semiconductor Compton camera," *IEEE Trans. Nucl. Sci.* **56**, 783–790 (2009).
40. S. Takeda et al., "Demonstration of in-vivo multi-probe tracker based on a Si/CdTe semiconductor Compton camera," *IEEE Trans. Nucl. Sci.* **59**, 70–76 (2012).
41. S. Watanabe et al., "The Si/CdTe semiconductor Compton camera of the ASTRO-H soft gamma-ray detector (SGD)," *Nucl. Instrum. Methods A* **765**, 192–201 (2014).
42. Y. Ichinohe et al., "The first demonstration of the concept of narrow-FOV Si/CdTe semiconductor Compton camera," *Nucl. Instrum. Methods A* **806**, 5–13 (2016).
43. K. Hayashi et al., "Radiation effect on the silicon semiconductor detectors for the ASTRO-H mission," *Nucl. Instrum. Methods A* **699**, 225–229 (2013).
44. T. Takahashi et al., "Application of CdTe for the NeXT mission," *Nucl. Instrum. Methods A* **541**, 332–341 (2005).
45. S. Watanabe et al., "High energy resolution hard X-ray and gamma-ray imagers using CdTe diode devices," *IEEE Trans. Nucl. Sci.* **56**, 777–782 (2009).
46. H. Tajima et al., "Performance of a low noise front-end ASIC for Si/CdTe detectors in Compton gamma-ray telescope," *IEEE Trans. Nucl. Sci.* **51**, 842–847 (2004).
47. H. Noda et al., "Thermal design of the hard x-ray imager and the soft gamma-ray detector onboard ASTRO-H," *Proc. SPIE* **9144**, 91445E (2014).
48. O. Toker et al., "VIKING, a CMOS low noise monolithic 128 channel frontend for Si-strip detector readout," *Nucl. Instrum. Methods A* **340**, 572–579 (1994).
49. S. D. Barthelmy et al., "The burst alert telescope (BAT) on the SWIFT Midex mission," *Space Sci. Rev.* **120**, 143–164 (2005).
50. P. Picozza et al., "PAMELA A payload for antimatter matter exploration and light-nuclei astrophysics," *Astropart. Phys.* **27**, 296–315 (2007).
51. M. Tavani et al., "The AGILE space mission," *Nucl. Instrum. Methods A* **588**, 52–62 (2008).
52. J. Kataoka et al., "Recent progress of avalanche photodiodes in high-resolution x-rays and gamma-rays detection," *Nucl. Instrum. Methods A* **541**(1–2), 398–404 (2005).
53. J. Kataoka et al., "Expected radiation damage of reverse-type APDs for the ASTRO-H mission," *J. Instrum.* **7**(6), P06001 (2012).
54. T. Saito et al., "Development of high performance avalanche photodiodes and dedicated analog systems for HXI/SGD detectors onboard the ASTRO-H mission," *Nucl. Instrum. Methods A* **699**, 230–234 (2013).
55. M. Ohno et al., "Development and verification of signal processing system of avalanche photo diode for the active shields onboard ASTRO-H," *Nucl. Instrum. Methods A* **831**, 410–414 (2016).
56. T. Mizuno et al., "Development and calibration of fine collimators for the ASTRO-H soft gamma-ray detector," *Proc. SPIE* **9144**, 91445F (2014).
57. K. K. Madsen et al., "Measurement of the absolute crab flux with NuSTAR," *Astrophys. J.* **841**, 56 (2017).
58. V. Schoenfelder et al., "Instrument description and performance of the imaging gamma-ray telescope COMPTEL aboard the Compton gamma-ray observatory," *Astrophys. J. Suppl. Ser.* **86**, 657–692 (1993).
59. N. Gehrels, E. Chipman, and D. A. Kniffen, "The Compton gamma ray observatory," *Astron. Astrophys. Suppl. Ser.* **97**, 5–12 (1993).

Hiroyasu Tajima is a professor of cosmic-ray physics at Nagoya University. He received his BS, MS, and PhD degrees in physics from Nagoya University in 1986, 1988, and 1991, respectively. He is the principal investigator (PI) of the SGD onboard the Hitomi satellite.

Shin Watanabe is an assistant professor of space astronomy and astrophysics at Institute of Space and Astronautical Science. He received his BS, MS, and PhD degrees in physics from the University of Tokyo in 1999, 2001, and 2004, respectively. He is the deputy PI of the SGD onboard the Hitomi satellite.

Yasushi Fukazawa is a professor of high-energy astrophysics at Hiroshima University. He received his BS, MS, and PhD degrees in physics from the University of Tokyo in 1991, 1993, and 1998, respectively. He is the deputy PI of the SGD onboard the Hitomi satellite.

Biographies for the other authors are not available.